3D elastic time-lapse full waveform inversion using multi-component seismic data

Espen Birger Raknes and Børge Arntsen, Norwegian University of Science and Technology*

SUMMARY

As a result of the increase in the computational power the recent years, we are now able to use the full waveform inversion (FWI) method in a full three dimensional isotropic elastic setting. We use a 3D implementation of the FWI method on time-lapse seismic multi-component data. We investigate two data-difference based approaches for estimating time-lapse effects directly in the P- and S-wave parameter models. In addition, we investigate how the inversion of the two parameter models should be performed, to reduce the total cost of the method. We find that both approaches are able to detect and estimate the time-lapse effects in the models. The inversion of the P- and S-wave velocity models in the monitor inversion may be performed simultaneously, as long as the baseline models are close to the true solution.

INTRODUCTION

A common assumption in wave propagation problems is that the subsurface is approximately an acoustic medium. Under these assumptions it is sufficient to use the acoustic wave equation (Aki and Richards, 2002) to model waves propagating through the medium. As a result of the increase in computational power the recent years, we now can leave the acoustic assumption behind, and instead use the elastic wave equations to model wave propagation in a medium. Moreover, it is possible to do this in a full three dimensional setup, within acceptable computing times.

The full waveform inversion (FWI) method is a technique for estimating parameters affecting wave propagation, and has been applied with success on both synthetic and real datasets (Virieux and Operto, 2009). The number of unknowns in the inverse problem, and thus the size of the parameter models, have increased. It is now possible to perform FWI in a full three dimensional setting.

Time-lapse seismic data contains information about changes in the subsurface, and has proven to be an effective tool in reservoir imaging and for monitoring of injected CO_2 in the subsurface (Biondi et al., 1996; Lumley et al., 2003). Two-dimensional implementations of FWI has been applied on time-lapse data with success (Zheng et al., 2011; Routh et al., 2012; Zhang et al., 2013; Raknes and Arntsen, 2014).

There have not been many attempts (as far as we know) on applying FWI on synthetic or real datasets using a full three dimensional implementation of the method. Warner et al. (2013) applied a full 3D anistropic acoustic implementation of FWI on a 4C ocean-bottom survey over a field in the North Sea. Butzer et al. (2013) applied 3D isotropic elastic FWI on a small-scale cross-well acquisition geometry using both synthetic and real datasets. Using FWI on time-lapse seismic data in a 3D setting is still under research.

In time-lapse full waveform inversion (TLFWI) at least two inversions must be performed. The computational cost of performing 3D elastic FWI is high, and therefore the number of iterations performed in the inversion should be held at a minimum, particularly when working with time-lapse data. The monitor inversion should use as much information as possible from the baseline inversion, and focus only on the differences in the datasets. Inverting for more than one elastic parameter is complicated, and in terms of computational cost, a natural question is how this should be done to reduce the total number of iterations in TLFWI.

The time-lapse images are obtained by subtracting the inverted parameter models from each of the datasets. Since FWI is ill-posed and nonlinear, and thus may get stuck in a local minimum, the method may introduce artifacts in the time-lapse image which may distort the interpretation. We like to call such noise in the images for *time-lapse artifacts*. It is important to find inversion schemes that tend to reduce the artifacts.

In this study, we investigate two different data-difference based approaches for performing 3D isotropic elastic TLFWI using synthetic ocean-bottom multi-component seismic data, where we estimate the P- and S-wave velocity models (denoted as V_p and V_s, respectively, in the following). In addition, we investigate different ways of performing the inversion to keep the total number of iterations at a minimum. To test our approaches we use two synthetic models. We find that we are able to detect and estimate time-lapse anomalies in the V_p and V_s models using both inversion approaches. In terms of computational cost, we find that the V_p and V_s models may be inverted simultaneously using the monitor dataset, as long as the inverted baseline models are sufficiently close to the solution.

TIME-LAPSE FULL WAVEFORM INVERSION

The theory that underlies FWI has been derived several times using different formulations, and we refer to Pratt (1999), Fichtner et al. (2006) and Virieux and Operto (2009) for a more detailed introduction to FWI than we have included here.

Full waveform inversion

The overall goal for FWI is to find a parameter model $\mathbf{m}$ which produce modeled data $\mathbf{u}$ which is close to some measured data $\mathbf{d}$. The foundation for the method is the assumption that synthetic data $\mathbf{u}$ can be generated using a numerical wave equation. Let $\mathscr{L}$ be the numerical wave operator which maps $\mathbf{m}$ from the model domain into the data domain. Then the synthetic data can be generated as follows

$$\mathscr{L}(\mathbf{m}) = \mathbf{u}. \tag{1}$$

If the inverse operator of $\mathscr{L}$, that is, the mapping from the data domain into the model domain, exists, then the solution to the problem is simply given as

$$\mathbf{m} = \mathscr{L}^{-1}(\mathbf{d}), \tag{2}$$

DOI http://dx.doi.org/10.1190/segam2014-0761.1

where $\mathscr{L}^{-1}$ is the inverse operator. In practice, however, it is not possible to find an explicit solver for the inverse operator.

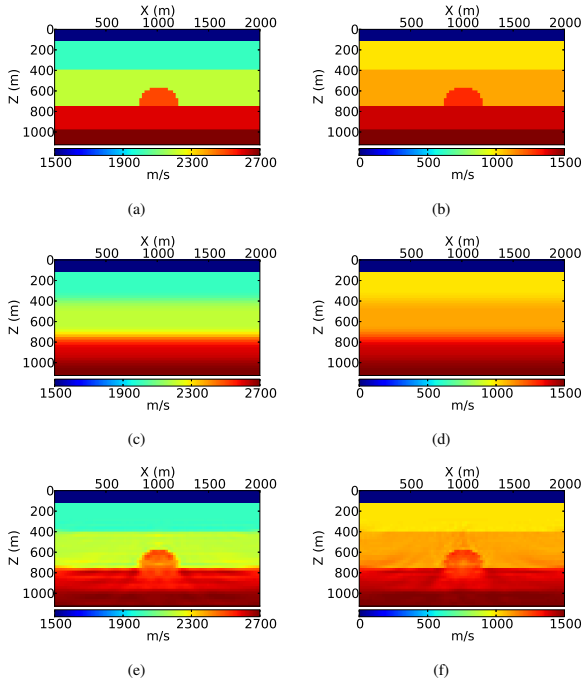

Figure 1: Vertical slice for example 1: (a) true V_p; (b) true V_s; (c) initial model V_p; (d) initial model V_S; (e) inverted baseline V_p; (f) inverted baseline V_s.

The standard way for solving the inverse problem, is to define a measure, denoted as $\Psi(\mathbf{m})$, between $\mathbf{u}$ and $\mathbf{d}$. This measure is often called for the objective (or misfit) functional. We require that the solution of the problem, that is, the point where $\mathbf{u}$ and $\mathbf{d}$ are equal, is an extreme point for $\Psi(\mathbf{m})$. Hence, the solution to the problem can simply be expressed as

$$\mathbf{m}' = \arg\min_{\mathbf{m}} \Psi(\mathbf{m}), \tag{3}$$

where $\mathbf{m}'$ is the model we are searching for. The inverse problem in equation 3 is non-linear and ill-posed.

The search for the extreme points of $\Psi(\mathbf{m})$ is done using an iterative optimization algorithm, written as

$$\mathbf{m}_{k+1} = \mathbf{m}_k - \alpha_k \mathbf{H}_k^{-1} \mathbf{g}_k, \tag{4}$$

where $\alpha_k > 0$ is the step length, $\mathbf{H}_k^{-1}$ is the inverse Hessian matrix, and $\mathbf{g}_k$ is the gradient of $\Psi(\mathbf{m})$ with respect to $\mathbf{m}$ at step k. To start the algorithm an initial model $\mathbf{m}_0$ is required, and the algorithm is run to some convergence criteria is fulfilled.

The crucial step in FWI is the computation of the gradient in equation 4. Using the adjoint state method (Tarantola, 1984; Mora, 1987) the gradients are efficiently calculated using equation 1.

In practice, the inverse Hessian matrix in equation 4 is complicated to compute, because it involves second-order derivates of the objective function. To overcome this problem, we use the L-BFGS algorithm (Nocedal and Wright, 2006) which is a quasi-Newton method that tries to estimate the inverse Hessian matrix using the gradients from previous iterations.

Time-lapse full waveform inversion

In time-lapse full waveform inversion (TLFWI) at least two inversions must be performed, and the time-lapse images are obtained by subtracting the inverted parameter models from the inversions.

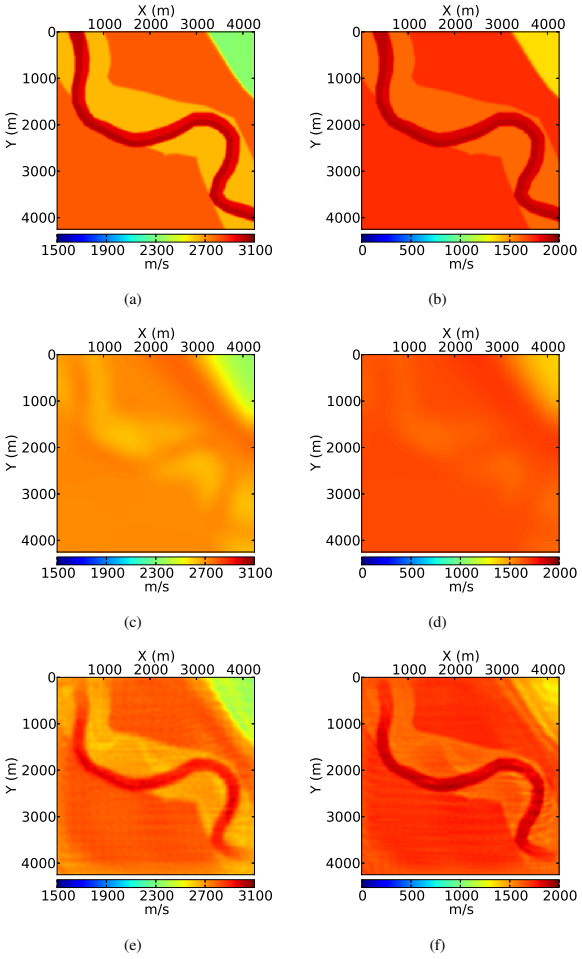

Figure 2: Horizontal slice at $z = 500$m for example 2: (a) true V_p; (b) true V_s; (c) initial V_p; (d) initial V_s; (e) inverted baseline V_p; (f) inverted baseline V_s.

We assume that we have two datasets $\mathbf{d}_{base}$ and $\mathbf{d}_{mon}$, where $\mathbf{d}_{base}$ and $\mathbf{d}_{mon}$ are the datasets from the baseline and monitor surveys, respectively. The datasets are assumed to have been aqcuired using identical source-receiver geometries and source function. Hence, we have perfect repeatability between the datasets.

The baseline inversion is common in both schemes and is performed using the standard least-squares functional

$$\Psi(\mathbf{m}) = \frac{1}{2} \sum_{(s,r)\in\mathbf{S}} \|\mathbf{u}(\mathbf{m};\mathbf{x}_r,\mathbf{x}_s) - \mathbf{d}(\mathbf{x}_r,\mathbf{x}_s)\|^2, \tag{5}$$

DOI http://dx.doi.org/10.1190/segam2014-0761.1

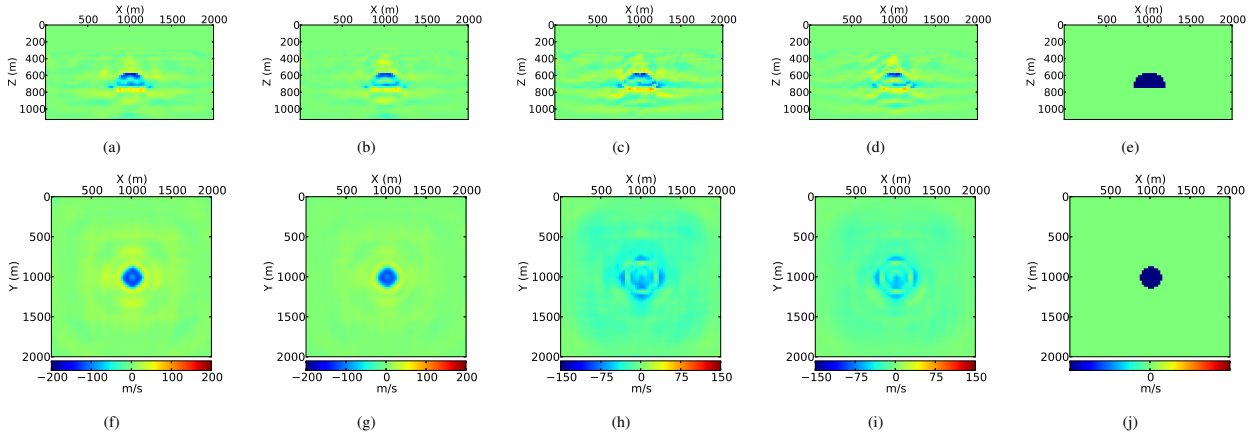

Figure 3: Time-lapse inversion results for example 1 (top: vertical slices at $y = 1000$m, bottom: horizontal slices at $z = 600$m): (a) and (f): V_p using app. 1; (b) and (g) V_p using app. 2; (c) and (h): V_s using app. 1; (d) and (i): V_s using app. 2; (e) and (j): true time-lapse effects (the magnitude for the V_p anomaly is -200 m/s and V_s is -150 m/s).

where $\mathbf{S}$ is the discrete set of all receiver and source enumerations, $\mathbf{x}_r$ and $\mathbf{x}_s$ are spatial location vectors of the receiver and source, $\mathbf{u}(\mathbf{m};\mathbf{x}_r,\mathbf{x}_s)$ is the modeled data at receiver r from source s, and $\mathbf{d}(\mathbf{x}_r,\mathbf{x}_s)$ is the measured data at the same position. The baseline inversion is run to convergence and a final model $\mathbf{m}_b$ is obtained.

In *approach 1*, the true monitor dataset is modified as follows before the inversion (Zheng et al., 2011)

$$\widehat{\mathbf{d}}_{mon} = \mathbf{u}_{base} + (\mathbf{d}_{mon} - \mathbf{d}_{base}), \tag{6}$$

where $\mathbf{u}_{base}$ is the inverted baseline dataset. The monitor inversion is run using

$$\Psi(\mathbf{m}) = \frac{1}{2} \sum_{(s,r)\in\mathbf{S}} \|\mathbf{u}(\mathbf{m};\mathbf{x}_r,\mathbf{x}_s) - \widehat{\mathbf{d}}(\mathbf{x}_r,\mathbf{x}_s)\|^2 \tag{7}$$

as the misfit functional. In *approach 2*, we use the following misfit functional

$$\Psi(\mathbf{m}) = \frac{1}{2} \sum_{(s,r)\in\mathbf{S}} \|\Delta\mathbf{d}(\mathbf{x}_r,\mathbf{x}_s) - \Delta\mathbf{u}(\mathbf{m};\mathbf{x}_r,\mathbf{x}_s)\|^2, \tag{8}$$

where $\Delta\mathbf{d} = \mathbf{d}_{mon} - \mathbf{d}_{base}$ and $\Delta\mathbf{u} = \mathbf{u}_{mon} - \mathbf{u}_{base}$.

There is a slightly difference between the two approaches. At the first iteration in approach 1, the value of the misfit is only the data difference. At the later iterations the inverted monitor data will be taken into account. In approach 2, on the other hand, the objective functional are completely driven by the differences of the differences. In that sense, this is a double-difference type of functional.

RESULTS

We assume that the subsurface is an elastic isotropic medium, so that the $\mathscr{L}$ in equation 1 is the elastic wave operator (Aki and Richards, 2002). We test the two time-lapse approaches on two models. In example 1 we use a simple five layered model, where we have introduced an half sphere in one of the layers (Figure 1). The half sphere acts as the time-lapse anomaly. In example 2 we use a model which is adapted from the SEG/EAGE Overthrust model, where we use a channel system at approximately 500m depth as the time-lapse anomaly (Figure 2). The grid sampling is 25m on the three axes in the examples. To avoid numerical aliasing we use a Ricker wavelet with center frequency 6Hz as the source signature. We put the density to the constant value of 1000 m/kg^3 in all our examples, and invert for V_p and V_s.

In example 1 we use an ideal receiver geometry, where we put receivers on a dense square grid (in total 4900 receivers) on the sea floor. We perform 324 shots with 100 m shot sampling in both directions. The source depth is 25 m. The initial model is a smooth version of the true model without the dome included. The baseline inversion results are given in Figure 1, while the time-lapse images are given in Figure 3.

In example 2 we use a more realistic OBC setup, using 16 cables with length 4km. The distance between each cable is 250 m. The total number of receivers are 2560. We perform 441 shots on a square grid, with shot sampling of 125m in both directions. The source depth is 25 m. The baseline inversion results are given in Figure 2, while the time-lapse images are given in Figure 4.

In terms of computational cost, we find that for example 1 we are able to invert for the V_p and V_s models simultaneously, both for the baseline and monitor datasets. There were no significant differences in the models obtain by inverting for the parameters on an one-by-one basis. For example 2, on the other hand, we find that that doing sequentially based inversion, where we first invert for V_p, then for V_s, and at last for both V_p and V_s, give the best results for the baseline dataset. For the monitor inversion, we find that it is sufficient to invert for V_p and V_s simultaneously in both examples. There were no significant differences between the results obtained using a sequentially based inversion scheme, and the simultaneously scheme for the monitor cases. Hence, we only needed to run

DOI http://dx.doi.org/10.1190/segam2014-0761.1

one inversion for the monitor case.

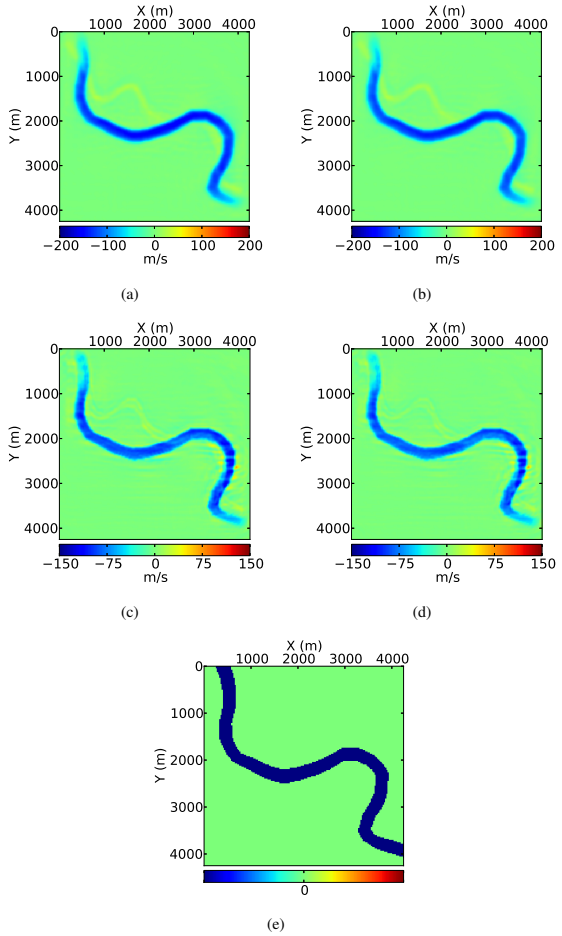

Figure 4: Time-lapse inversion results for for example 2. Horizontal slices at $z = 500$m: (a) V_p using app. 1; (b) V_p using app. 2; (c) V_s using app. 1; (d) V_s using app. 2; (e) true time-lapse effect (the magnitude for the V_p anomaly is -200 m/s and V_s is -150 m/s).

DISCUSSION

Our examples demonstrate that it is possible to use a full three-dimensional implementation of FWI to invert for V_p and V_s using multi-component ocean-bottom data. In both our examples, the baseline inversion was able to get final inverted models within the accepted resolution. In our trial runs of the baseline inversion, we tried different starting models. The strong surface waves, particularly the Scholte waves, were complicated to estimate using FWI. Therefore, the initial model had to be close to the true model in the parts close to the sea floor.

Both approaches were able to reveal time-lapse anomalies in the V_p and V_s models. In example 1 we observe that the top of the anomalies are detected, but the areas in the curved part of the dome are somewhat lost (Figure 3). This can be explained by the relative short offset of the receivers, and the shape of the anomaly. For example 2 (Figure 4), we observe that both approaches are able to detect the time-lapse anomaly in the channel system. If we compare the time-lapse images obtained with the two approaches, we observe that they are close to be equal. The difference that is possible to observe, is the amplitude of the time-lapse anomalies; the trend is that the images created with approach 1 have a amplitude slightly closer to the true amplitude, compared to the images obtained using approach 2. The time-lapse artifacts are small using both approaches.

We tried different ways of performing both the baseline and monitor inversion for V_p and V_s. It is interesting that a simultaneously approach where one invert for V_p and V_s was successful for the baseline dataset in example 1 and not in example 2. This may be explained by the fact that the model in example 1 is fairly simple, compared to the model in example 2, in combination with the distance of the initial model from the true model. For the monitor inversion, the simultaneously approach was successful in both examples. Thus, the inverted models for the baseline case was so good, that the inversions did not get stuck in a local minimum far away from the solution. Hence, having a good estimate of the baseline models, may reduce the overall runtime of TLFWI.

It is worth mentioning that the two time-lapse approaches presented here have strong requirements on the acqusition geometry of the datasets. To consider the data differences, one need to require that the receivers are put on the same positions in space in the baseline and monitor surveys. In a permanent OBC setup this is easy, while using conventional streamer geometries it is more tricky. Therefore, the data difference based inversion schemes may not be used in cases where the time-lapse datasets are not acquired using the same source-receiver geometries.

CONCLUSION

We have investigated two data difference based approaches for estimating time-lapse anomalies in the V_p and V_s models using OBC datasets and a 3D isotropic elastic implementation of FWI. We find that both approaches are able to detect the time-lapse anomalies for both parameter models. We have, in addition, investigated computational cost of TLFWI. We find that as long as the baseline models are sufficiently close, the V_p and V_S models may be inverted for simultaneously in the monitor inversion.

ACKNOWLEDGMENTS

This work has been produced with support from the BIGCCS Centre, performed under the Norwegian research program Centres for Environment-friendly Energy Research (FME). The authors acknowledge the following partners for their contributions: ConocoPhillips, Gassco, Shell, Statoil, TOTAL, GDF SUEZ and the Research Council of Norway (193816/S60). We also thank the ROSE consortium and their sponsors for support.

DOI http://dx.doi.org/10.1190/segam2014-0761.1

http://dx.doi.org/10.1190/segam2014-0761.1

EDITED REFERENCES

Note: This reference list is a copy-edited version of the reference list submitted by the author. Reference lists for the 2014 SEG Technical Program Expanded Abstracts have been copy edited so that references provided with the online metadata for each paper will achieve a high degree of linking to cited sources that appear on the Web.

REFERENCES

Aki, K., and P. G. Richards, 2002, Quantitative seismology, 2nd ed.: University Science Books.

Biondi, B., C. Deutsch, R. Gundesø, D. Lumley, G. Mavko, T. Mukerji, J. Rickett, and M. Thiele, 1996, Reservoir monitoring: A multi-disciplinary feasibility study: 66th Annual International Meeting, SEG, Expanded Abstracts, 1775–1778, http://dx.doi.org/10.1190/1.1437860.

Butzer, S., A. Kurzmann, and T. Bohlen, 2013, 3D elastic full-waveform inversion of small-scale heterogeneities in transmission geometry: Geophysical Prospecting, **61**, no. 6, 1238–1251, http://dx.doi.org/10.1111/1365-2478.12065.

Fichtner, A., H.-P. Bunge, and H. Igel, 2006, The adjoint method in seismology: I Theory: Physics of the Earth and Planetary Interiors, **157**, no. 1-2, 86–104, http://dx.doi.org/10.1016/j.pepi.2006.03.016.

Lumley, D., D. C. Adams, M. Meadows, S. Cole, and R. Wright, 2003, 4D seismic data processing issues and examples: 73rd Annual International Meeting, SEG, Expanded Abstracts, 1394–1397.

Mora, P., 1987, Nonlinear two-dimensional elastic inversion of multioffset seismic data: Geophysics, **52**, 1211–1228, http://dx.doi.org/10.1190/1.1442384.

Nocedal, J., and S. J. Wright, 2006, Numerical optimization, 2nd ed.: Springer Science–Business Media.

Pratt, R. G., 1999, Seismic waveform inversion in the frequency domain, Part 1: Theory and verification in a physical scale model: Geophysics, **64**, 888–901, http://dx.doi.org/10.1190/1.1444597.

Raknes, E. B., and B. Arntsen, 2014, Time-lapse full-waveform inversion of limited-offset seismic data using a local migration regularization: Geophysics, **79**, no. 3, WA117–WA128, http://dx.doi.org/10.1190/geo2013-0369.1.

Routh, P., G. Palacharla, I. Chikichev, and S. Lazaratos, 2012, Full wavefield inversion of time-lapse data for improved imaging and reservoir characterization: 82nd Annual International Meeting, SEG, Expanded Abstracts, http://dx.doi.org/10.1190/segam2012-1043.1.

Tarantola, A., 1984, Inversion of seismic reflection data in the acoustic approximation: Geophysics, **49**, 1259–1266, http://dx.doi.org/10.1190/1.1441754.

Virieux, J., and S. Operto, 2009, An overview of full-waveform inversion in exploration geophysics: Geophysics, **74**, no. 6, WCC1–WCC26, http://dx.doi.org/10.1190/1.3238367.

Warner, M., A. Ratcliffe, T. Nangoo, J. Morgan, A. Umpleby, N. Shah, V. Vinje, I. Štekl, L. Guasch, C. Win, G. Conroy, and A. Bertrand, 2013, Anisotropic 3D full-waveform inversion: Geophysics, **78**, no. 2, R59–R80, http://dx.doi.org/10.1190/geo2012-0338.1.

Zhang, F., C. Juhlin, M. Ivandic, and S. Lüth, 2013, Application of seismic full waveform inversion to monitor CO_2 injection: Modelling and a real data example from the Ketzin site, Germany: Geophysical Prospecting, **61**, no. S1, 284–299, http://dx.doi.org/10.1111/1365-2478.12021.

Zheng, Y., P. Barton, and S. Singh, 2011, Strategies for elastic full waveform inversion of time-lapse ocean bottom cable (OBC) seismic data: 81st Annual International Meeting, SEG, Expanded Abstracts, 4195–4200, http://dx.doi.org/10.1190/1.3628083.

DOI http://dx.doi.org/10.1190/segam2014-0761.1